Landslides (2018) 15:1745–1759
DOI 10.1007/s10346-018-0994-0
Received: 13 October 2017
Accepted: 13 April 2018
Published online: 30 April 2018

Amin Askarinejad · Devrim Akca · Sarah M. Springman

Precursors of instability in a natural slope due to rainfall: a full-scale experiment

Abstract A full-scale landslide-triggering experiment was conducted on a natural sandy slope subjected to an artificial rainfall event, which resulted in mobilisation of 130 m^3 of soil mass. Novel *slope deformation sensors* (SDSs) were applied to monitor the subsurface pre-failure movements and the precursors of the artificially triggered landslide. These fully automated sensors are more flexible than the conventional inclinometers by several orders of magnitude and therefore are able to detect fine movements (< 1 mm) of the soil mass reliably. Data from high-frequency measurements of the external bending work, indicating the transmitted energy from the surrounding soil to these sensors, pore water pressure at various depths, horizontal soil pressure and advanced surface monitoring techniques, contributed to an integrated analysis of the processes that led to triggering of the landslide. Precursors of movements were detected before the failure using the horizontal earth pressure measurements, as well as surface and subsurface movement records. The measurements showed accelerating increases of the horizontal earth pressure in the compression zone of the unstable area and external bending work applied to the slope deformation sensors. These data are compared to the pore water pressure and volumetric water content changes leading to failure.

Keywords Landslide monitoring · Natural hazards · Slope movements · Slope deformation sensors · Slope stability · Unsaturated soils · Geotechnical physical modelling · Rainfall

Introduction

Shallow, fast-moving landslides triggered by rainfall cause significant damage to infrastructure and affect many lives all over the world, particularly in mountainous regions. The dependency of the soil shear strength on effective stress and the pore water pressure suggests a strong correlation between the frequency of landslides and the hydrological conditions in a region, which is directly controlled by the climate (Borgatti and Soldati 2010). Accordingly, it is predictable that the probable increase in the number of extreme climatic events (Frei et al. 2006; Crozier 2010; Huggel et al. 2012; Collins et al. 2013; Gariano and Guzzetti 2017), coupled with concentration of population and infrastructure in mountainous regions, will lead to an increase in casualties associated with landslides in the future.

A better understanding of the triggering mechanisms, early detection of the soil mass movements, accompanied by an efficient evacuation strategy, are crucial for disaster mitigation. However, complex interactions between many geomechanical (e.g. Harp et al. 1990; Alonso et al. 2003; Springman et al. 2003; Take et al. 2004; Towhata et al. 2006; Borja and White 2010; Cascini et al. 2010; Yildiz et al. 2015; Soga et al. 2016; Elia et al. 2017; Tang et al. 2018), hydrological (e.g. Montgomery et al. 2009; Krzeminska et al. 2012) and hydrogeological (e.g. McDonnell 2003; Brönnimann et al. 2013) processes can lead to the instability of a slope, all of which need to be taken into account when designing landslide prediction tools. Frequent measurement of deformations and shear band depth in unstable slopes can be used to estimate the possible volume of an eventual landslide. However, surface and/or subsurface displacement measurements cannot be used as numerical indicators of the safety conditions of the slope because the mechanical relationships between displacements, future failure mechanism(s) and associated safety factor cannot be investigated properly (Urciuoli 2002). Several researchers, such as Griffiths et al. (2011), Urciuoli et al. (2007), Picarelli (2000) and Leroueil et al. (2009), suggest that the safety of a slope subjected to pore water pressure increase is influenced significantly by the stresses parallel to the slope. Therefore, reliable measurements of the horizontal stresses in the slope provide valuable information about the state of stability of the soil mass. Hence, frequent and accurate measurements of displacement should be combined with the rain, pore pressure and horizontal soil pressure data to increase the reliability of predictions.

Slope inclinometers are the instruments most commonly used to monitor subsurface deformations in "extremely slow to slow" moving landslides (based on the classification of Cruden and Varnes (1996)), for which a relatively large monitoring interval (a few measurements per day or week) would suffice. However, the precursors of failure in sandy slopes might happen relatively close to the final stages of triggering the landslide and therefore conventional slope inclinometers are unsuitable (Ochiai et al. 2004; Picarelli et al. 2006).

Alternatively, ShapeAccelArray/Field (SAAF) systems are capable of collecting data at a maximum sampling frequency of 128 Hz, which makes them suitable for dynamic measurements (Bennett et al. 2009). They consist of an articulated chain of triaxial MEMS (micro-electro-mechanical systems) accelerometers installed on successive elements (segments) each 0.305 or 0.500 m long (Abdoun et al. 2010). They are normally installed inside PVC pipes of 25 and 32 mm inner and outer diameters, respectively. Therefore, the fine movements prior to the failure cannot be captured reliably if the casing has a high bending stiffness compared to the surrounding soil (Arenson et al. 2002; Buchli et al. 2016). Moreover, they cannot easily be used to monitor movements of shallow layers above the bedrock, given the minimum required segment length.

Soil deformation sensors (SDSs) were developed to monitor the subsurface movements of a natural silty sand slope at a frequency of 100 Hz and to investigate the precursors of landslides induced by rainfall (Askarinejad and Springman 2017). The measurements are based on recording and processing the bending strains along a flexible plate installed in the soil. The bending stiffness of these sensors is 300 times and 50 times less than that of the casings of

slope inclinometers and SAAF sensors, respectively. A detailed comparison between the three subsurface denomination methods is reported by Askarinejad and Springman (2017).

Features of the pre-failure movements of a natural slope subjected to heavy rainfall events are presented in this paper, and the results of the changes in bending strains along the SDSs are analysed to calculate the subsurface deformation profiles. These measurements are compared to the results of the surface movements recorded and computed using the photogrammetric method.

The horizontal pressures inside the soil body were also measured by earth pressure cells (EPCs) to obtain a spatial distribution of horizontal stresses at a frequency of 100 Hz. A network of hydrological, geotechnical and geophysical sensors was also used to monitor hydraulic aspects of the slope behaviour, in response to two extreme artificial rainfall events (Askarinejad et al. 2012b).

The main objective of this paper is to analyse the way in which the landslide was triggered and started to move, using a combination of data from the sensors and the photogrammetric methods. One of the focuses of this analysis will be on the rate of the changes in various hydromechanical parameters leading to the landslide and whether the data from SDSs and EPCs could reveal the location of the failure.

Test site

The 38° steep slope had an area of approximately 300 m^2 and was located 380 m above sea level (m asl) in the northern part of Switzerland, close to Ruedlingen village, where several shallow landslides had occurred during, and following, extreme rainfall events in May 2002. The landscape shows many signs of creeping surficial deposits. The geological structure of the region mainly consists of Sandstone and Marlstone, which was deposited in the foreland basin of the Alps, containing alternate depositions (Platt 1992; Sinclair 1997; Labhart 2005). Outcrops of Sandstone, springs, wet zones and ancient landslide deposits have been mapped in the region. The test site lies at the interface of the Sandstone and Marlstone (Brönnimann 2011). The bedrock surface lies between 0.5 m and more than 5 m depth and was laterally inclined with a shallow convex form in the lower part of the slope (Figs. 1 and 2). Fissures, which were parallel to the river Rhine, were mapped in the bedrock. These results were obtained from extensive geophysical surveys using the electrical resistivity tomography (ERT) method during the experiments (Lehmann et al. 2013).

The lateral root distribution and root strength were estimated experimentally to quantify the root reinforcement. The root distribution was characterised based on the root diameter classes and frequency (Schwarz 2011). Maximum root reinforcement was measured at approximately 2–3 m away from tree trunks. Figure 3b shows the spatial distribution of maximal contribution of the roots to the shear strength of the soil in the study area estimated with the root bundle model (Pollen and Simon 2005; Schwarz et al. 2010; Cohen et al. 2011).

Soil characterisation

The main characteristics of the soil from the test slope are summarised in Table 1. Several disturbed and undisturbed samples

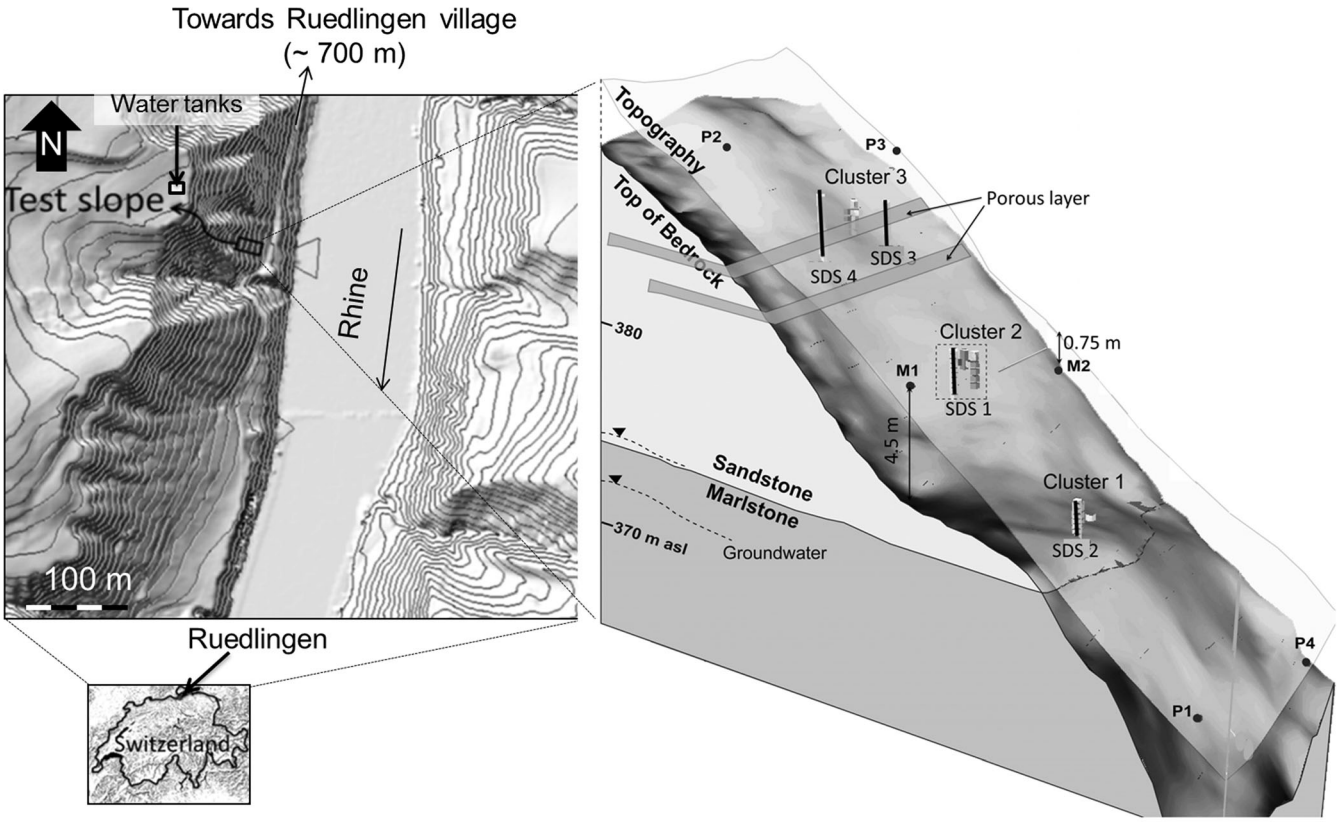

Fig. 1 Left: The location of the test slope and topography of the region (The interval between elevation contours is 5 m. The relief and topography map is taken from http://www.sh.ch/). Right: Shape of the bedrock, positions of the sensor cluster and the slope deformation sensors (after Brönnimann 2011)

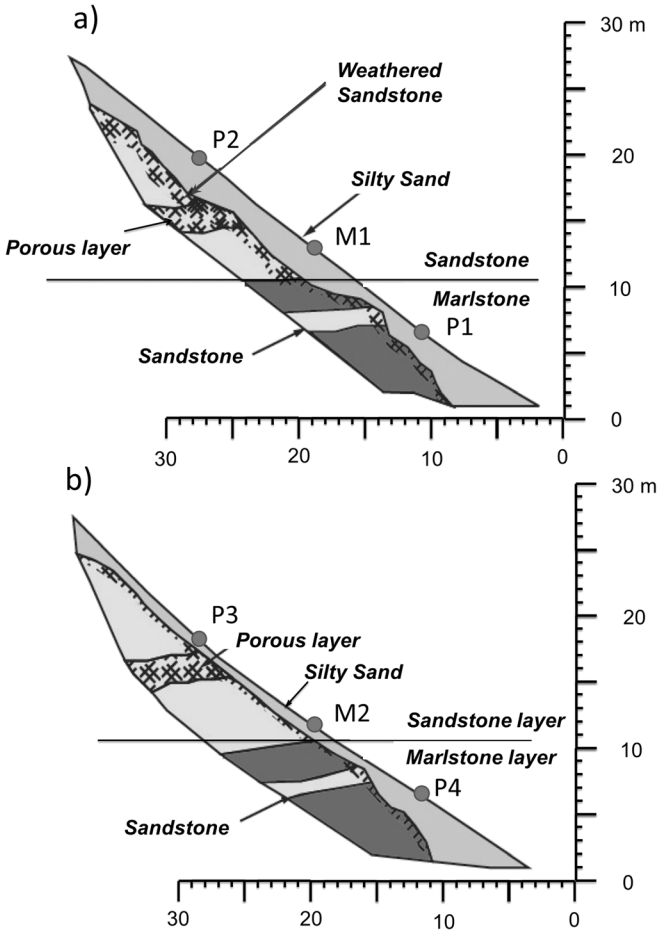

Fig. 2 Schematic of the bedrock layers and the soil depth on two sides of the slope. **a** Left-hand side. **b** Right-hand side (looking upslope)

were taken from six test pits, which were located on the north and south sides of the slope between 5 and 20 m away from the borders of the test area. The sampling depth was up to 2 m. About 20 undisturbed samples for oedometer, saturated hydraulic conductivity, and water retention curve tests were taken by pressing 84.2 mm inner diameter thin-walled (20 mm high) rings into the ground. A flat platform was prepared in the test pit at each depth, and two vertically stacked rings were pushed into the soil very gently. The soil inside the lower ring formed the sample to be tested whereas the upper ring contained excess soil extruded during the process. Blocks of soil (approximately 100 mm × 100 mm × 100 mm) containing the rings were extracted and taken to the laboratory. The soil blocks were covered tightly with plastic sheets to avoid evaporation of pore water pressure and to maintain the in situ water content during transportation. The surrounding soil was then trimmed from the top and bottom of the lower ring, and the samples were prepared for testing. The value of in situ void ratio of the soil was determined for 12 samples. Larger sampler tubes, with 170 mm diameter and a length of 400 mm, were used to collect undisturbed samples for triaxial tests. No cementation has been detected between the soil particles, so major slope stabilising effects were provided by suction and root reinforcement. Wetting and drying branches of the water retention curve (WRC) of a natural undisturbed sample taken from site were determined using the axis translation technique (Delage et al. 2008; Marinho et al. 2008) (Fig. 4a). The saturated hydraulic conductivity of soil was determined to be approximately 5×10^{-6} m/s (Askarinejad et al. 2015). The hydraulic conductivity function (HCF) of partially saturated soil ($K_r = K_{unsat}/K_{sat}$) was derived using the *instantaneous profile method* (Daniel 1982) (Fig. 4a) (Askarinejad et al. 2012a).

A series of unsaturated constant shear triaxial tests (Brand 1981) were performed to replicate the stress path that a soil element experiences during the rise of pore water pressure in a slope, during and/or after a rainfall event (Fig. 4b). The testing apparatus and the measurement ranges of the sensors were controlled and set to comply with the low confining stresses required for these tests. The unsaturated specimens with initial void ratios of 1.08 and 0.86 and gravimetric water contents of 16.5 and 16.6% were prepared using the moist tamping method. They were anisotropically consolidated following initial isotropic consolidation to 12.3 kPa and 14.27 kPa. The looser specimen ($e_o = 1.08$) experienced a slightly higher consolidation stress ratio ($\eta = 1.2$, $\eta = q/p'$, where $q = \sigma'_a - \sigma'_r$ and $p' = (\sigma'_a + 2\sigma'_r)/3$, σ'_a is the effective axial stress and σ'_r is the effective radial stress applied in the triaxial cell), while the consolidation stress ratio for the specimen with lower initial void ratio was $\eta = 1.06$.

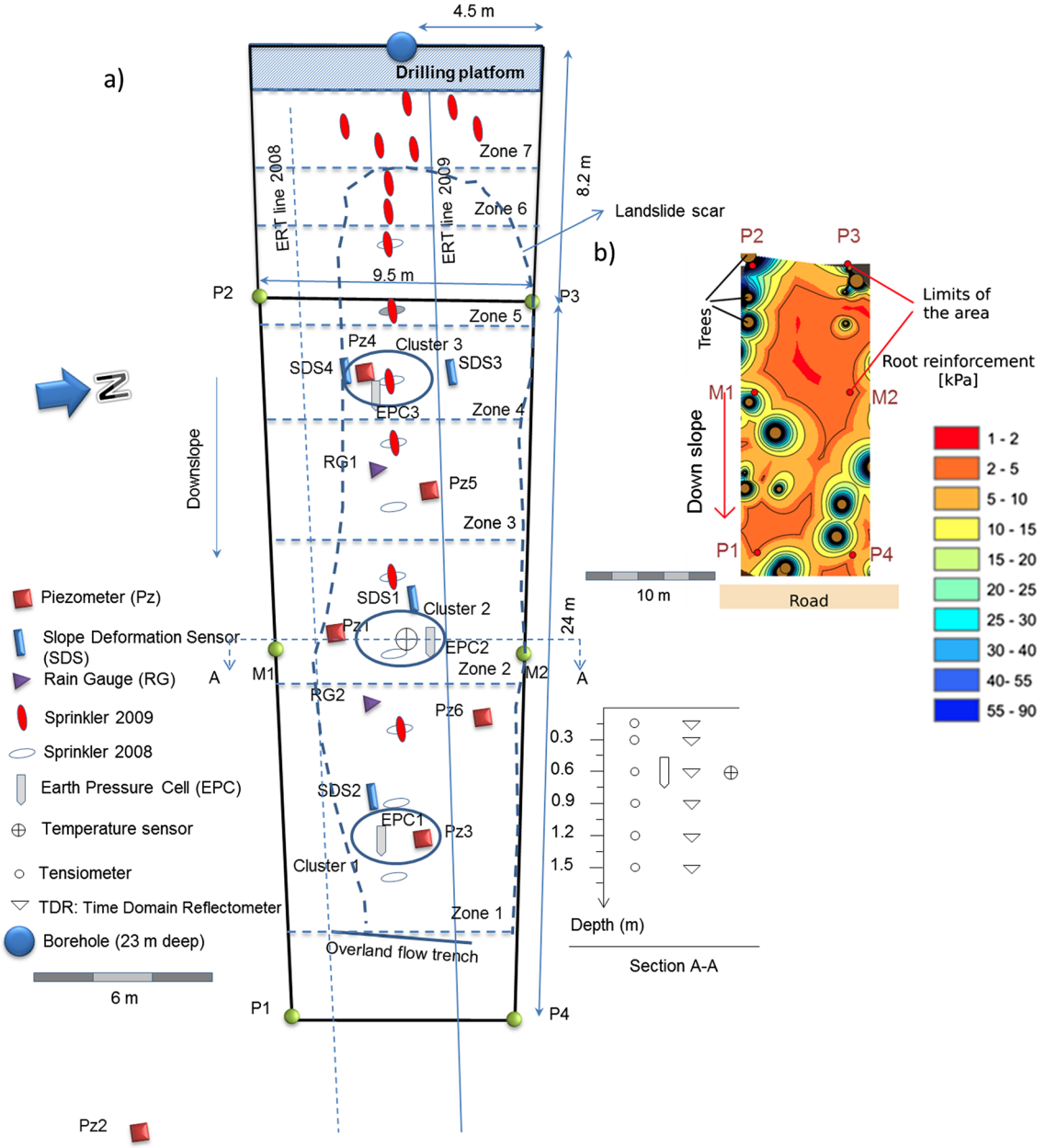

Fig. 3 **a** Instrumentation and different raining zones in the Ruedlingen test site; ERT electrical resistivity tomography (after Askarinejad 2013). **b** Spatial distribution of maximal root reinforcement in the study area (after Schwarz 2011). The instrumentation arrangement as shown in cross section A-A is also applied to other instrumentation clusters

The actuator applied 2.5 kPa higher deviatoric stress to the looser sample and then the internal feedback loop regulated it to the set value. Subsequently, water was injected into the specimens via the lower pore pressure valve. Thus, the mean effective stress decreased while the deviator stress and cell pressure remained constant. The decrease in the mean effective stress was controlled at a rate of 0.001 kPa/s.

The average value of volumetric water content was calculated based on the water balance of the specimen (difference between injected and extruded water from the specimen) and the volumetric changes. The suction was calculated according to the corresponding water retention curve. The actuator decreased the pore pressure slightly and then increased it, i.e., a small amount of water was sucked out of the specimen at the beginning and then water was injected into the specimen. This malfunction of the actuator is attributed to the low values of pore pressures in these tests and also to the interaction process between the pore pressure transducer and the motor of the actuator.

Accordingly, an increase in the mean effective stress was measured before the start of shearing in both tests. This increase in the mean effective stress was higher for the looser sample to about 5 kPa. Subsequently, the stress path of both specimens maintained

Table 1 Physical properties of the soil

Property	Value
Particle sizes, D_{10}, D_{30}, D_{50}, D_{60}: mm	0.015, 0.07, 0.13, 0,19
Specific gravity, G_s (–)	2.6
Minimum dry unit weight, γ_{min}: kN/m^3	12.5
Maximum dry unit weight, γ_{max}: kN/m^3	15.3
Plasticity Index (%)	9.9
Soil classification (USCS) (ASTM 2006)	Medium- to low-plasticity silty sand (SM)
Mean in situ void ratio (–)	0.9
Mean in situ water content (%)	19.6

constant deviator stress with decreasing mean effective stress until they experienced a decrease in the deviator stress at a stress ratio of 1.47, in both cases. The results suggest that the stress ratio ($\eta_{U\text{-}CSD} = 1.47$) attained at failure is generally higher than the critical state stress ratio determined by conventional drained or undrained triaxial tests (Casini et al. 2010). The soil specimen is following an unloading path, and therefore the higher value of the stress ratio at failure in this stress path compared to the critical stress ratio is due to the tendency of dilative behaviour in the specimen at very low confining pressures.

Instrumentation

The instrumentation setup was planned either to measure or to be able to derive profiles of pore water pressure, volumetric water content (at depths of 0.15 to 1.5 m), groundwater level, horizontal soil pressure, precipitation intensity, electrical resistivity of the ground and surface and subsurface deformations. The instruments were installed in three main "instrumentation clusters" (Fig. 3a). The volumetric water content was measured using time domain reflectometers (TDRs), which were calibrated for the silty sand of the test site. The specifications of the sensors are listed in Table 2.

The depth of the failure surface and the profile of subsurface movements of the soil mass were determined using four slope deformation sensors. The main part of a SDS is a slender aluminium (ALMg1) plate with a rectangular cross section (40 × 2 mm^2). Pairs of strain gauges, with pre-determined spacings, were installed on both sides of the plate as "half Wheatstone bridges" (Wheatstone 1843) to eliminate the temperature effects and to measure the bending strain at different depths. The sensors were installed in boreholes, which were drilled at pre-defined locations on the slope (Figs. 1 and 3) to a depth of 200 mm into the weathered bedrock. The SDS length was specified according to the depth of the bedrock at the location. The installed length above the bedrock of each SDS is reported in Table 3.

The inclination of the deformed sensor, with respect to its initial position, can be calculated according to the measured bending strains (Askarinejad 2009). The deflection of the plate was derived from the inclination curve by integration based on the assumption that the main Aluminium body of the SDS remains elastic. Boundary conditions were defined by the fixed lower end of the sensor, with zero base deflection and rotation. The details regarding the calibration of these sensors, limit of the measurement range and accuracy of the measurements are discussed by Askarinejad and Springman (2017).

Three *press-in* Glötzl pressure transducers (*EPE/P model*) were pushed into the soil at pre-defined locations up to a depth of 0.60 m to measure the horizontal earth pressure and pore water pressures. The sensors are composed of pressure pads, filled with de-aired oil, connected to a pressure transducer. The pore water pressure is measured using a pore pressure transducer connected to a de-aired oil saturated reservoir. The reservoir is in contact with the surrounding soil via a porous stone. The sensor has been tested to measure negative pore pressures reliably up to 8 kPa.

Landslide-triggering experiments

Artificial rainfall was applied to the selected slope over a period of 4.5 days in October 2008, with an average intensity of 15 mm/h for the first 2.5 days and 30 mm/h for the last 2 days. However, no failure was observed. A second attempt was made in March 2009 after implementation of a range of measures such as relocating the distribution of the sprinklers to provide more rainfall to the upper part of the slope (Fig. 3a), where less soil reinforcement due to vegetation was present (Fig. 3b). Artificial rainfall was applied by means of 14 oscillating garden sprinklers (Gardena Aqua-zoom 250). The lower sprinklers

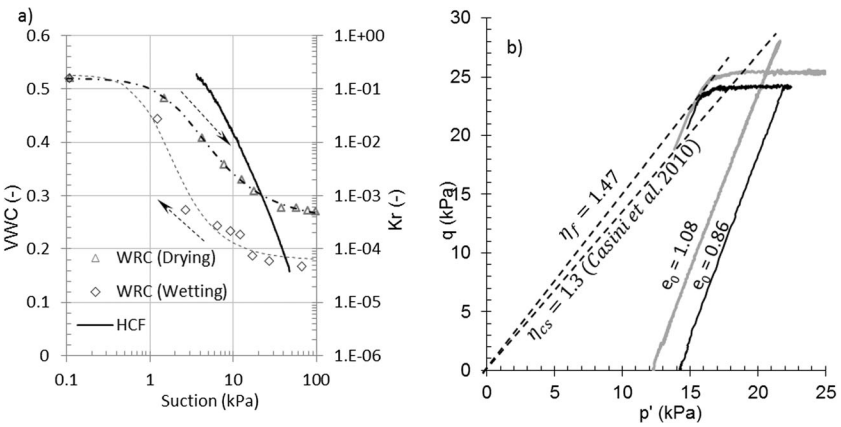

Fig. 4 **a** Water retention curve (WRC) of natural undisturbed samples from the test site determined using the axis translation technique and hydraulic conductivity function (HCF) for reconstituted Ruedlingen soil, derived with the instantaneous profile method (VWC volumetric water content). **b** Stress paths during consolidation and shearing of specimens in unsaturated constant shear triaxial tests

Table 2 Specifications of the sensors

Measurement	Sensor	References	Calibration	Measurement range	Accuracy
Pore water pressure	Standard tensiometer	*Soil moisture (2710L)* and *Keller AG*	Linear	− 90 to 100 kPa	± 0.5 kPa
Volumetric water content	TDR100	Campbell Scientific, Inc	Soil-specific calibration based on Ledieu et al. (1986)	0 to 1 (m^3/m^3)	± 3.0% volumetric water content
Volumetric water content	TDR	Decagon EC5	soil-specific calibration	0 to 1 (–)	± 0.02 (–)
Groundwater table	Piezometer	Keller-Druck	Linear	0 to 100 kPa	± 0.1 kPa
Bending strain	Strain gauges installed on the SDS	LK11-HBM	Linear	− 50 to 20 $m\varepsilon$	± 1 $\mu\varepsilon$
Horizontal earth pressure	Press-in pressure transducers	Glötzl (EPE/P model)	Linear	0 to 500 kPa	± 1 kPa
Subsurface soil movement	SDS	Self-designed	Linear (Askarinejad and Springman 2017)	0 to 25 mm[a]	± 5% of the measurement

[a] Depending on the thickness of the shear band (Askarinejad and Springman 2017)

experienced higher hydraulic heads as the water was supplied from water tanks above the slope (i.e. water tanks in Fig. 1); therefore, the spacing between the sprinklers was smaller in the upper part of the slope. The discharge from each sprinkler was calculated based on its installation location on the slope and hydraulic losses within the hoses and at the connections. The slope was partitioned into seven zones (Fig. 3), and the amount of discharged water was calculated for each zone, according to the zonal area and number of sprinklers in it. The average rain intensity applied was about 10 mm/h, while it was just under 20 mm/h on the uppermost part of the slope and less than 5 mm/h in the lower part (Fig. 5). Two precipitation intensity-duration thresholds ($I = a \cdot D^b$, where I is the rain intensity (mm/h), D is rain duration (h), and a and b are model parameters) for shallow landslides and debris flows determined for Switzerland (Zimmermann et al. (1997) ($a = 32$, $b = -0.7$)) and for the central Europe region (Guzzetti et al. 2007) ($a = 15.56$, $b = -0.7$)) are compared in Fig. 6 with the monthly precipitation records from the meteorological stations close to Ruedlingen for the period of 1864–2009 and hourly precipitation records for the period of 2000–2009, the single local record of May 2002 (Fischer et al. 2003) and two artificial rainfall events from the Ruedlingen slope monitoring and landslide-triggering experiments in October 2008 and March 2009, respectively.

The failure mechanism of the slope after the artificial rainfall event of March 2009 incorporated a mixture of "rotational" movement in the upper part of the slope, becoming "translational" in the middle portion, according to the classification suggested by Varnes (1978). The "debris slide" turned into a "debris flow" within about 30 s after triggering, with a maximum velocity of about 3 m/s, which fits in the velocity category of "very rapid" (class 6) according to Cruden and Varnes (1996). The velocity of the debris flow was measured by image analysis of the captures from the photogrammetry cameras. The length of the failure zone was about 17 m, the width was 7 m and the depth varied between 0.3 and 1.3 m. The failure occurred at the interface of the soil and the bedrock on the right-hand side (looking upslope) and was located inside the soil mantle on the left-hand side (Figs. 3 and 6). The lateral inclination of the bedrock, from the right to the left side of the slope, resulted in development of the perched water table on top of the bedrock at a faster rate on the right-hand side, which caused the initiation of the failure. Moreover, discharge of water from the porous layers inside the bedrock (exfiltration) (Figs. 1b and 7) was detected at two locations at the back of the failure scar.

Table 3 Length and location of the strain gauge pairs on the SDSs

Sensor no.	Installed Length above the bedrock (m)	Location	Strain gauges depths from soil surface (m)
1	2.080	Cluster 2	1.610–1.367–1.124–0.881–0.638–0.395–0.255–0.115
2	1.800	Cluster 1	1.400–1.230–1.060–0.890–0.720–0.550–0.380–0.210
3	1.800	Cluster 3	1.400–1.230–1.060–0.890–0.720–0.550–0.380–0.210
4	2.800	Cluster 3	2.400–2.085–1.770–1.455–1.140–0.825–0.510–0.195

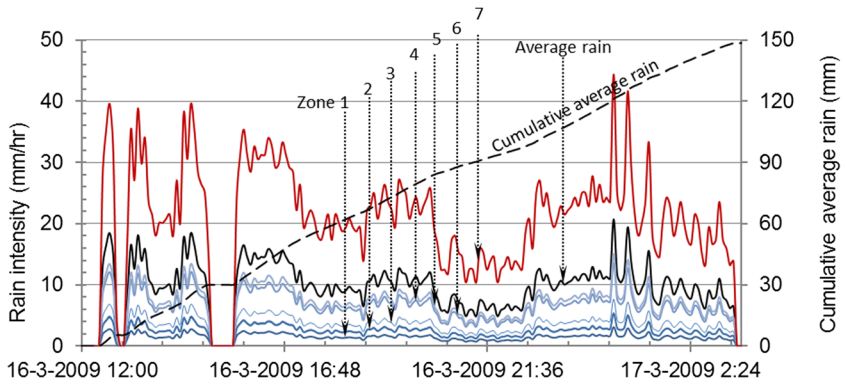

Fig. 5 Artificial rainfall intensity applied to the different zones on the Ruedlingen slope during the landslide triggering experiment

Hydraulic responses of the slope

Changes in pore water pressure

Profiles of the PWP at different clusters during the rainfall event are shown in Fig. 8. The increase in pore water pressure, representing infiltration of the wetting front, occurred faster in the upper part of the slope (cluster 3) compared to the middle and the lower parts, due to higher rain intensities at the top of the slope.

The profile of pore water pressure did not show significant changes from time 14 h until failure at time 15 h in clusters 1 and 2. However, the pore water pressure decreased at depths of 0.30, 0.60, 1.20 and 1.50 m with an average value of 0.7 kPa in cluster 3 (Fig. 9a).

Changes in the volumetric water content

The value of volumetric water content is used in combination with the pore water pressure to determine the effective stress of the soil in unsaturated condition (Bishop 1959; Bishop and Blight 1963) and hence the shear strength of the material, as shown in Eq. (1). Therefore, monitoring of this parameter is necessary to evaluate the stability of an unsaturated slope.

$$\sigma' = (\sigma - u_a) + \chi(u_a - u_w) \quad (1)$$

where u_a is pore air pressure, and $(\sigma - u_a)$ is named as normal *net stress*; $(u_a - u_w)$ is *matric suction* and χ is an *effective stress parameter*, which is related to the amount of moisture content in an unsaturated soil (Alonso et al. 1990; Toll 1990; Khalili and Khabbaz 1998; Nuth and Laloui 2008; D'Onza et al. 2011).

The volumetric water content at a depth of 0.60 m of the slope in cluster 3 increased from 28% to around 45% during the rainfall event, while this changed from 25% to a maximum value of 59% at a depth of 1.20 m (Fig. 9b). The TDRs at 0.60 and 0.90 m responded to the rainfall after 60 and 100 min, respectively. However, the deeper TDRs at 1.20 and 1.50 m showed increases in VWC after 100 and 140 min. The TDR at 1.20 m measured higher values of water content, compared to the TDR at 1.50 m. This can be due to difference in porosity of the soil at these two depths or to a local perched water table at the depth of 1.20 m, as indicated by the response in cluster 3 after 3 h (Fig. 8c). The TDR at a depth of 1.20 m, which was the nearest instrument to the slip surface, measured a decrease in volumetric water content after about 10 h of measuring an almost constant VWC. This occurred about 1 h before the failure.

Mechanical responses of the slope

Surface movements of the slope before landslide

A multi-image convergent network was set-up with four cameras to monitor surface movements using the close-range photogrammetric method. The images were captured at a rate of five frames per second (fps). The camera calibrations were performed using a self-calibrating bundle adjustment, both in the laboratory and under out-door conditions. Target tracking and image measurement used an adaptive sub-pixel cross-correlation method, both of which were implemented in two in-house software packages (BAAP and SGAP) to compute 3D coordinates of the target points,

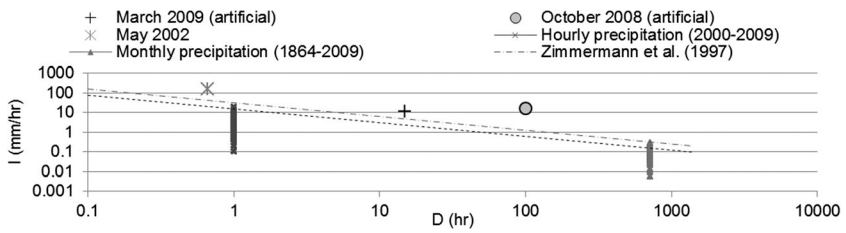

Fig. 6 Two rainfall intensity-duration thresholds for shallow landslides and debris flows compared with the monthly and hourly precipitation records, the single local record of May 2002 (Fischer et al. 2003) and two artificial rainfall events of Ruedlingen slope monitoring and landslide-triggering experiments in October 2008 and March 2009, respectively

Fig. 7 Post event record of the landslide and relative location of the soil deformation sensors with respect to the destabilised soil mass

respectively. An average 3D point-positioning precision of ± 18 mm was achieved (Akca et al. 2011). The three-dimensional coordinates of 63 white target points, which were pegged to the ground over the slope, were determined during the experiment.

The relative displacements of the target points are illustrated graphically in Fig. 10. Computations on the images from the start of sprinkling until 23 min before the failure were made at 1 frame per hour (fph), and show relatively small planar movements, both down and across the slope (Fig. 10a). The upper right quadrant started to move downslope at a higher speed during the next 22 min before failure, reaching a maximum value of 400 mm in the horizontal plane and 300 mm in the vertical direction at some points (Fig. 10b). The average velocity of surface planar movements was calculated to be 0.5 mm/s during this 22 min period, with a maximum of 1.97 mm/s. The upper right quadrant of the slope moved downslope during the last 30 s before the failure, with an average velocity of 140 mm/s. A maximum speed of

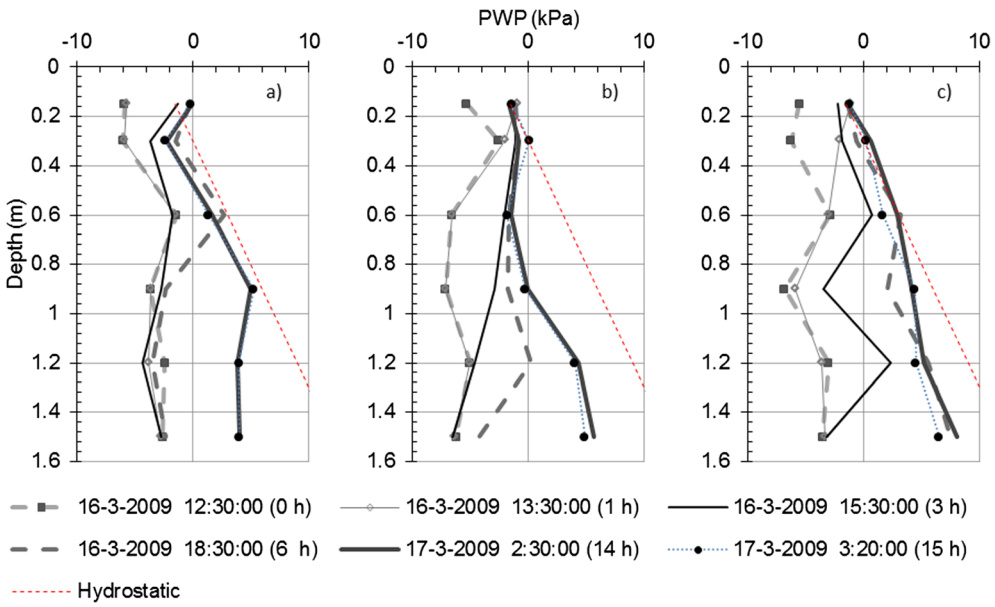

Fig. 8 Profiles of the PWP at **a** cluster 1, **b** cluster 2, and **c** cluster 3 during the landslide-triggering experiment. (Time begins from the start of the artificial rainfall 16.03.2009 12:30)

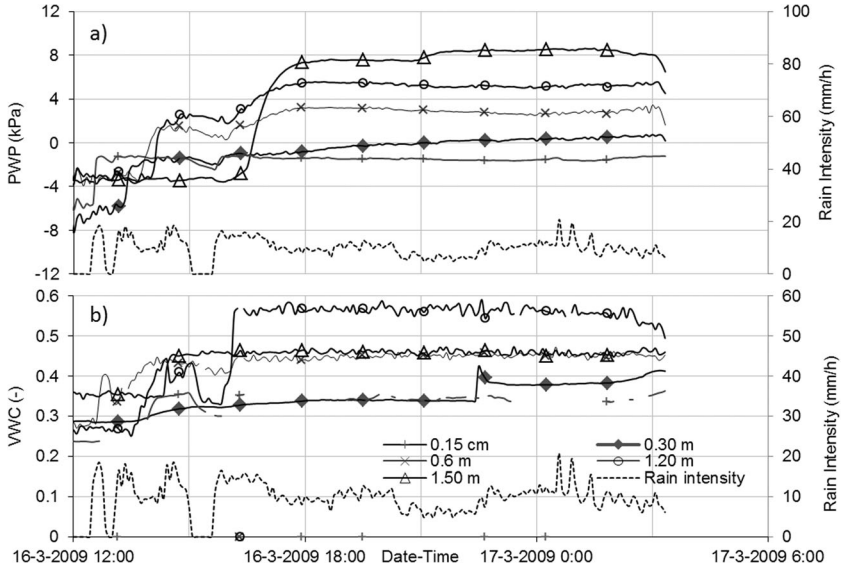

Fig. 9 Hydraulic responses of the upper part of the slope (cluster 3) to rainfall. **a** Changes in the pore water pressure (PWP). **b** Changes in the volumetric water content (VWC)

1.0 m/s was reached at some locations on the right-hand side of the sliding zone (Fig. 10c).

Depth of the failure surface and profile of the subsurface movements

Three of the slope deformation sensors (SDS3, 4 and 1) were inside the failed area. The movement of the slope was derived, based on data from SDS4 and SDS1. The grouted base of the SDS3 was totally removed by the landslide as the failure occurred at the interface of the soil and bedrock at the location of this sensor.

There is a change in the sign of bending strain at the point where the failure surface hits the slope deformation sensors (Fig. 11). Accordingly, the depth of the failure surface can be estimated by determination of the depths of adjacent strain gauges with different bending strain signs.

The bending strain measurements at two different depths of 1.14 and 1.455 m along the SDS4 are shown in Fig. 12a. The strain gauges located at these two points recorded similar but mirrored trends of changes in bending strains; both measurements indicated two local peaks before they start to accelerate about 30 min before failure. The occurrence of the two local peaks in bending strains might be due to the development of a shallower slip surface at a depth of 0.5 m (Fig. 13) and its interaction with the deeper and major shear band in the soil mass.

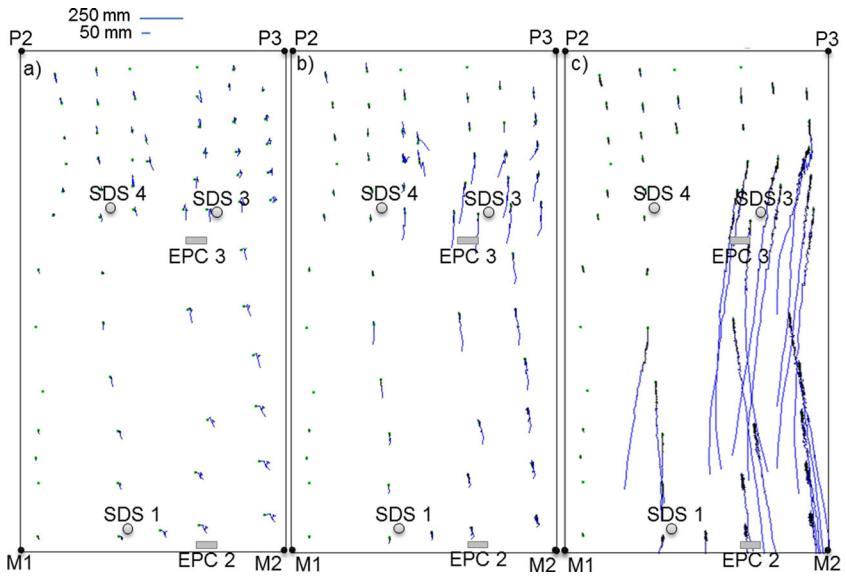

Fig. 10 Displacement of the target points on the slope surface. **a** Between the start of sprinkling and 23 min before failure. **b** During the last 22 min before failure. **c** During failure. (Locations of M1, M2, P2 and P3 are shown in Figs. 1, 2 and 3)

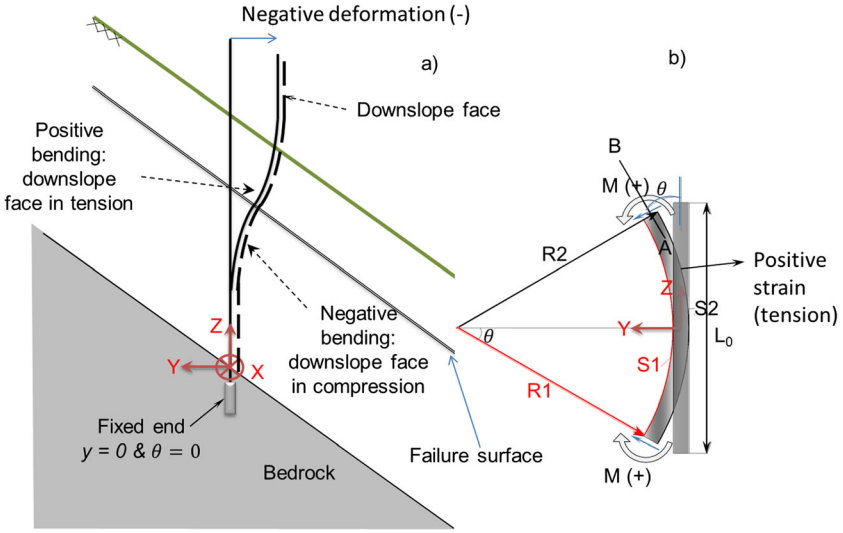

Fig. 11 Slope deformation sensors. **a** Coordinate system and sign convention. **b** Initial condition and deformed shape

The SDS4 deformation profiles are shown in Fig. 13. Two slip surfaces can be identified by tracking shape changes in the deformed SDS4: the first at a depth of 0.50 m and the dominant one subsequently at 1.30 m depth. This agrees well with field observations after failure (small image in Fig. 13). These two slip surfaces have interactive effects on the behaviour of the SDS4, due to differences in the initiation time and speed of propagation.

The depth of the shear zone close to the toe of the failure surface (cluster 2, Figs. 3 and 7) can be determined by tracking the bending strain variations of SDS1, during the last seconds before failure at depths of 0.395 and 0.638 m (Fig. 12b). Initially, the paths of strains versus time diverge gradually, with an increasing rate, reaching peaks at both depths a few seconds before failure. This observation indicates the development of a shear zone at SDS1 at about 0.5 m depth during the latter phases of the active landslide.

Integrated analysis of the landslide event

The behaviour of the slope is analysed based on the measurements of four slope deformation sensors, three earth pressure cells, three piezometers and six tensiometers located inside the failed zone. The changes in rain intensity measured by the rain gauge in cluster 3, which was in the initiation zone, are shown in Fig. 14a, together with the air temperature and soil temperature at 0.60 m depth in cluster 2.

Piezometric heights at three locations inside the failed area are shown in Fig. 14b. All of the *Keller Druck* piezometers were installed using the sand filter method. A borehole was made to the specified depth and a closed end standpipe was inserted inside the borehole. Holes of typical diameter of 2–5 mm at tip of the standpipe had been drilled and were protected by a cloth filter against blockage by fine particles. Sand was placed as a filter around the piezometer, which was positioned at the end of the pipe. A clay plug was formed on top of the sand. However, Pz4, which is installed in cluster 3 close to SDS4 (Fig. 3), at a depth of 3 m, functioned more like a *well*, i.e. the gap between the piezometer casing and the borehole wall is filled with gravel, linking the borehole hydraulically to the piezometer tube. This sensor shows increases in the water level about 4 h after the start of rainfall. The piezometric height at Pz4 stabilises to a value of 1.6 m thereafter, with the phreatic surface at 1.4 m below the surface at Pz4.

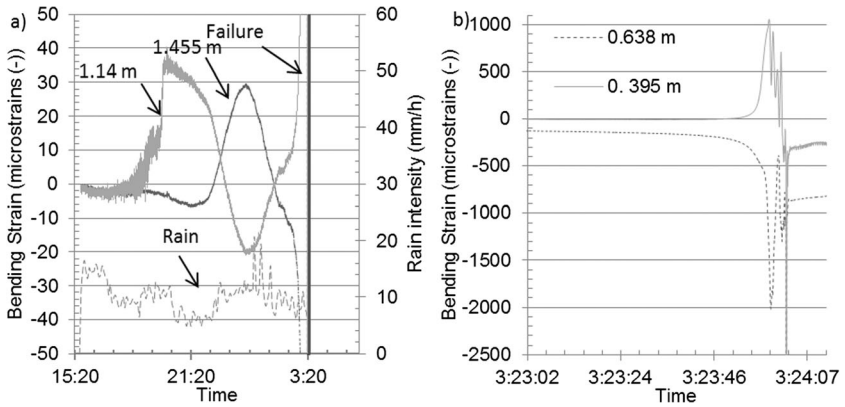

Fig. 12 **a** Changes in bending strain at depths of 1.14 and 1.455 m (above and below the eventual failure surfaces, respectively) along SDS 4. **b** Changes in the bending strain at depths of 0.395 and 0.638 m of SDS1 installed in cluster 2 during the last seconds before the failure

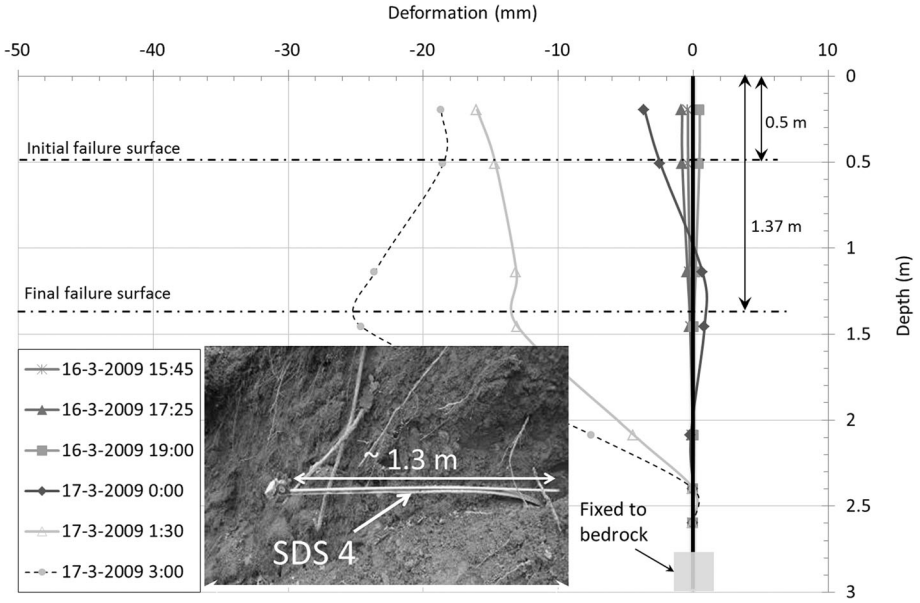

Fig. 13 Deformation profile of SDS4 during the landslide triggering experiment. The small photo on the lower part of the graph shows the deformed SDS after failure

Pz 5 is located between clusters 2 and 3, at a depth of 1.4 m, and shows an increase in the water table 1.5 h after Pz4, before staying almost stable at a piezometric height of 0.8 m (i.e. phreatic surface 0.6 m below ground level). Pz1 is installed in the middle of the field, at a depth of 4 m and measures a water table of 0.25 m from the beginning of the experiment. However, 6 h after the start of the rainfall, it showed a drop of 0.15 m, followed by a steady increase to 0.47 m until 2 h before the failure, when a similar drop of about 0.16 m was measured. Likewise,

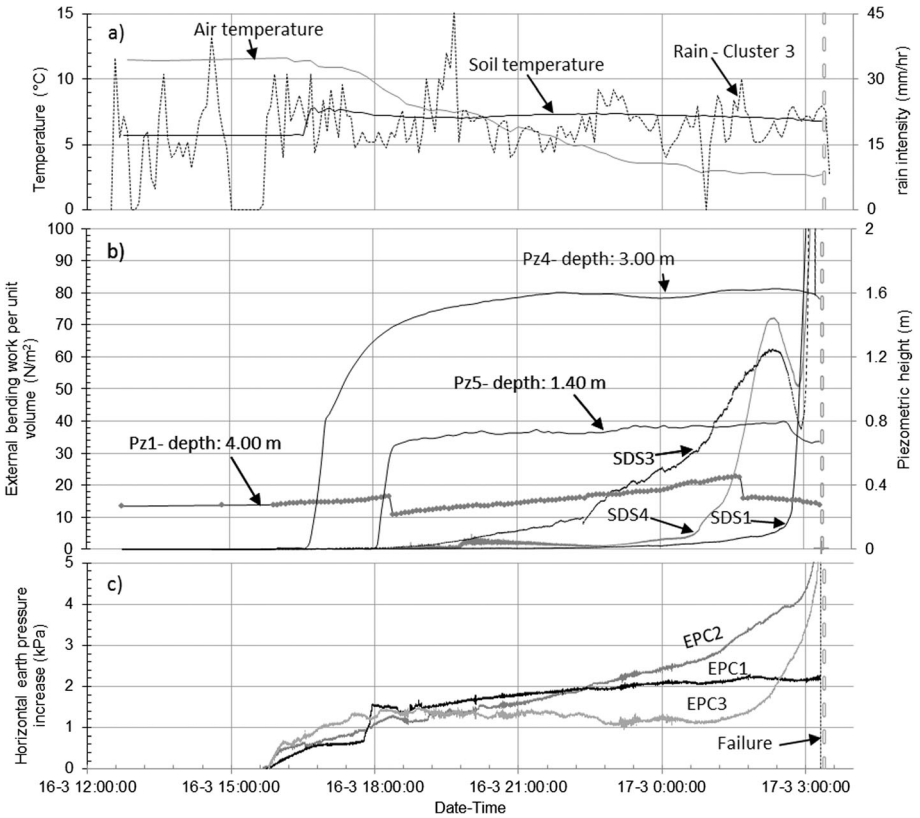

Fig. 14 **a** Rainfall measured at cluster 3, soil temperature at 60 cm depth at cluster 2 and air temperature measured at the upper part of the slope. **b** External bending work per unit volume of slope deformation sensors and Piezometer measurements. **c** Changes in horizontal earth pressure

Pz4 and Pz5 showed decreases in the piezometric heights about 55 and 20 min before failure, respectively. The time of the decrease in hydraulic head measured by Pz4, which was the closest piezometer to the slip surface, approximately coincides with the time that the bending strains accelerated in SDS3 and SDS4. The observed decreases in volumetric water content (measured by the TDR at a depth of 1.20 m, Fig. 9b), piezometric levels and pore water pressure (measured by the tensiometer at a depth of 1.50 m, Fig. 9) can be attributed either to dilation of the soil at the failure surface or to development of some other forms of drainage through the ongoing slope deformations. Dilation can occur as the confining effective stresses at the shear band decrease due to increase of the pore water pressure with accompanying increase in void ratio and hence permeability. Casini et al. (2013) have also reported dilative behaviour of the silty sand samples from the experiment site during triaxial tests. These triaxial tests were performed on reconstituted specimens which were consolidated anisotropically and then sheared by decreasing mean effective stress at constant axial load. Similar observation of abrupt decreases in pore pressure prior to failure has been reported by Harp et al. (1990) in two landslides triggered on natural slopes. They attributed these drops to the piping of fine-grained soil particles.

The changes in horizontal earth pressure at a depth of 0.6 m are illustrated in Fig. 13c for all clusters. Earth pressure cell installed in cluster 1 (EPC1) in the bottom part of the slope showed a sharp increase of about 1 kPa during the early stages of the rainfall, with continual gradual increase, thereafter.

However, EPC2, which is in the compression zone of the eventual failed area, showed increases from the start of the measurements, which accelerated about 2 h (time 17–03 01:10:00), and subsequently 30 min, before failure. The first event coincided approximately with the time when the external bending work applied to SDS3 accelerated towards the local peak (Fig. 14b).

The readings of the earth pressure cell at the top of the slope (EPC3; cluster 3) showed lower values than those measured by the other two sensors. This can be attributed to proximity of this cell to the extension area of the failure; therefore, the pressures were lower. However, this cell also showed an exponential increase in horizontal earth pressure (EPC3) starting about 2 h before failure occurred (time 17–03 01:10:00).

Changes in the external bending work per unit volume of the slope deformation sensors (Appendix) are presented in Fig. 14b. Higher values of external bending work per unit volume of SDS3 compared to SDS4 indicate larger movements on the right-hand side of the field, initially. This hypothesis is supported by the results of surface movement measurements using the photogrammetric method (Fig. 10).

Analysis of the earth pressure changes during the large slope movements

Horizontal earth pressure, pore water pressure and the lateral earth pressure coefficient (K) at a depth of 0.60 m in three clusters, during the last 35 s of the slope movement, are depicted in Fig. 15. This time period covers the initiation and development of large

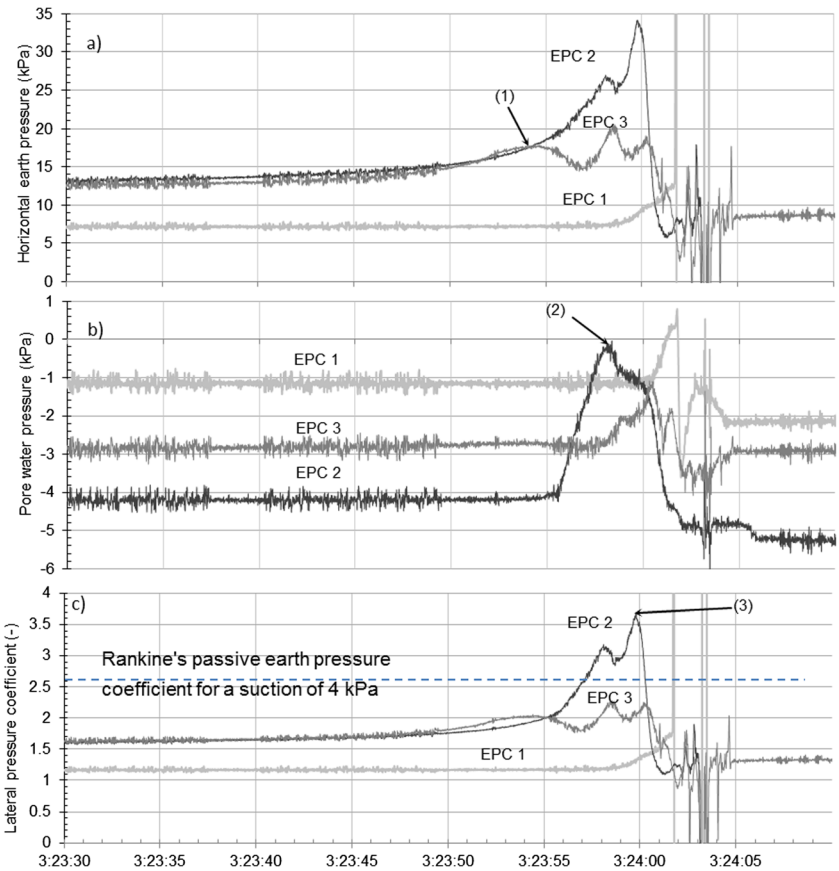

Fig. 15 Data measured at a depth of 0.6 m in all three clusters during the last 40 s of experiment before landslide. **a** Horizontal soil pressure. **b** Pore water pressure. **c** Horizontal earth pressure coefficient

movements of the soil mass. These movements started in the upper part of the slope and propagated downwards. Higher pressures are recorded in clusters 2 and 3, compared with cluster 1, which was within the runout area of the debris (Fig. 3). Horizontal earth pressures at clusters 2 and 3 are similar until 3:23:54 (time point (1) in Fig. 15a), measuring 16 kPa before the ground accelerated near cluster 2. This increase of total pressure has resulted in an increase of pore water pressure by ~ 4 kPa in this cluster (time point (2) in Fig. 15b, time 3:23:58). The depth of the failure surface at the location of cluster 2 was determined by the SDS1 to be around 0.5 m (Fig. 12b). Therefore, the measurements recorded by the EPC2 are regarded as the pressure fluctuations in the soil mass close to the shear band.

The value of lateral earth pressure coefficient (K) was calculated using Eq. (2):

$$K = {}^{\sigma_h'}\Big/_{\sigma_v'} \tag{2}$$

where σ_h' and σ_v' are horizontal and vertical effective stresses. Bishop stress (Bishop 1959; Bishop and Blight 1963) was used (Eq. 1) and the *effective stress parameter* (χ), was assumed to be equal to degree of saturation, as suggested by Öberg and Sällfors (1997) and Jommi (2000). The value of degree of saturation was calculated from the volumetric water content and the porosity of the soil (Fig. 9b and Table 1). The value of K increases from 1.6 to a maximum of 3.6, as failure developed at time 3:23:59.7 (time point (3) in Fig. 15c) in the lowest compression zone (cluster 2). This peak is followed by a sudden decrease of earth pressure both at clusters 2 and 3, whereas the values of pore water pressure and K are both increasing in cluster 1. At the same time, the horizontal pressure and the value of K fluctuated in cluster 3, resulting in alternating relaxation and compression. The theoretical value of passive earth pressure at a depth of 0.6 m in a slope of 38° inclination, with 4 kPa of suction as measured by the pore pressure transducer (Fig. 15b), can be estimated using Rankine's theory of earth pressure. The value of suction contributes as an apparent cohesion in the formulation suggested by Rankine (1857).

The fluctuating changes of the horizontal earth pressure and pore water pressure in cluster 3 might be due to a *concertina effect* caused by alternating extension and compression as the slope fails. The fluctuating changes in pore water pressure and horizontal earth pressure can be attributed to several other factors, such as development of interacting unstable blocks along the failed area, non-uniformity of the surface of the bedrock, heterogeneity of the soil and pull out and/or breakage of the roots at the base and side shear zones.

Summary and conclusions

Artificial rain was applied to a 38° steep forested slope in Northern Switzerland with an average intensity of 10 mm/h. A landslide of ~ 130 m^3 in volume was triggered after 15 h of rainfall. Slope deformation sensors were used to monitor the subsurface pre-failure movements of the soil mantle. These sensors are more flexible than the conventional inclinometers, such as SAAF and standard slope inclinometers, by several orders of magnitude and therefore are able to detect fine movements of the soil mass prior to failure. The data can be logged at high temporal resolution (100 Hz) fully automatically. The depth of the failure surface was successfully determined based on the location of adjacent strain gauges, which showed divergent tilts along the sensors.

The pre-failure movements have been determined from the changes in the bending strains along the sensor. However, the measurements of subsurface displacements can be less reliable at large shear displacements along the failure surface (Askarinejad and Springman 2017). This is caused by excessive bending of the sensor at the slip surface. The external bending work per unit volume of each sensor was determined as an indicator of the transmitted mechanical energy from the surrounding soil. However, it should be noted that the stability of the slope is directly related and influenced by the changes in the pore water pressure in the soil mass and the measurement of the transmitted energy from the surrounding soil to the sensors can be merely regarded as an indication of the relative subsurface movements in various parts of a slope.

Data from measurements of the pore water pressure, horizontal soil pressure and multi-camera surface monitoring (5 fps) contribute to an integrated analysis of the hydromechanical responses of the slope to a heavy rainfall event. The hydraulic and mechanical behaviour of the slope illustrated close interaction between the bottom-up saturation of the soil mass, together with the pore pressure development through rainfall infiltration, rate of movements and the coefficient of horizontal earth pressure. The measurements showed accelerating increases of the horizontal soil pressure, measured in a compression zone of the failing mass, approximately 2.5 h and more significantly ~ 23 min before the failure.

The subsurface measurements of slope deformations and earth pressures indicate that the upper section of the slope sheared, developing a tension crack behind it and compressing the ground in the middle of the slope in two phases, until the lateral earth pressure coefficient (K) reached passive failure at the end of phase two, while ground pressures reduced temporarily at the initiation zone. Flow of water from the bedrock could be detected at this stage, which confirmed the measured increases in pore pressures at the interface of the soil and bedrock. Subsequently, the sliding block at the initiation zone also accelerated. Concertina behaviour then developed between blocks in the upper and lower parts of the landslide, with differing rates of acceleration and earth pressure development. A linear increase in horizontal earth pressure was measured in the eventual runout area of the landslide, after failure occurred in the upper areas of the slope, but this never reached the passive limit.

Acknowledgements

Additional resources were provided by the ETH Research Fund and EU project of SafeLand (EU FP7 grant agreement no. 226479). We are grateful to the Ruedlingen Council, especially Mrs. K. Leutenegger and M. Kern, the fire station, the farmers, foresters and communities of Ruedlingen and Buchberg; E. Bleiker, C. Brönnimann, F. Casini, M. Denk, S. Durot, A. Ehrbar, F. Gambazzi, R. Herzog, M. Iten, P. Kienzler, J. Laue, P. Lehmann, G. Michlmayr, F. Morales, M. Nuth, D. Or, C. Rickli, R. Rohr, A. Schmid, M. Schwarz, M. Sperl, M. Staehli, K. Steiner, B. Suski, A. Volkwein, A. von Botticher, C. Wendeler, F. Wietlisbach and the late Adrian

Zweidler are thanked for their various contributions to this project. The authors thank the editor and reviewers for their thoughtful and detailed comments that have helped greatly in improving the manuscript.

Funding information This research was funded by the Competence Centre for Environment and Sustainability (CCES) within the framework of the Swiss project: Triggering Rapid Mass Movements (TRAMM).

Appendix. External bending work

The external work done on a beam with length L due to bending can be defined as (Freudenthal 1966):

$$W = \int_v (\sigma_{zz}\varepsilon_{zz}) dA dz \tag{3}$$

where σ_{zz} and ε_{zz} are the axial stress and strain due to bending, respectively; v is the volume of SDS, and A is the area of the cross section of the bent element.

The bending strain at each depth of the cross-section (y) is related to the inverse of the radius of curvature (κ) according to beam theory for pure bending:

$$\varepsilon_{zz}(y) = -y \cdot \kappa, \kappa = 1/R \tag{4}$$

$$M = \int_A \sigma_{zz} \cdot y \cdot dA \tag{5}$$

where R is the radius of curvature due to bending moment (M). Equation 6 is derived by combining the three Eqs. 3 to 5:

$$W = \int \left[\int_A \sigma_{zz} \cdot y \cdot dA\right] \kappa \, dz = \int_0^L M\kappa \, dz \approx \sum_1^n M\kappa \, \Delta L \tag{6}$$

where n is the number of strain gauges, and ΔL is the spacing of the strain gauges. The value of the external bending work per unit volume of SDS is calculated as

$$U = W/v \tag{7}$$

where U is the external bending work per unit volume of the bending part, and v is volume of the SDS.

References

Abdoun T, Bennet V, Dobry R, Koelewijn A, Thevanayagam S (2010) Real-time monitoring of full-scale levee testing Proc. 7th Int. Conf. on Physical Modelling in Geotechnics, Zurich, 2:1711–1176

Akca D, Gruen A, Askarinejad A, Springman SM (2011) Photogrammetric monitoring of an artificially generated landslide International Conference on Geo-information for Disaster Management (Gi4DM), Antalya, Turkey, Published on CD-ROM only

Alonso EE, Gens A, Josa A (1990) A constitutive model for partially saturated soils. Géotechnique 40(3):405–430

Alonso EE, Gens A, Delahaye C (2003) Influence of rainfall on the deformation and stability of a slope in overconsolidated clays: a case study. Hydrogeol J 11(1):174–192

Arenson L, Höelzle M, Springman SM (2002) Borehole deformation measurements and internal structure of some rock glaciers in Switzerland. Permafr Periglac Process 13:117–135

Askarinejad A (2009) A method to locate the slip surface and measuring subsurface deformations in slopes 4th International Young Geotechnical Engineers' Conference, Alexandria, Egypt, 171–174

Askarinejad A (2013) Failure mechanisms in unsaturated silty sand slopes triggered by rainfall. DSc thesis No. 21423, ETH Zurich

Askarinejad A, Springman SM (2017) A novel technique to monitor the subsurface movements of landslides. Can Geotech J. https://doi.org/10.1139/cgj-2016-0338

Askarinejad A, Beck A, Casini F, Springman SM (2012a) Unsaturated hydraulic conductivity of a silty sand with the instantaneous profile method. In E-Unsat 2012, Unsaturated soil: research and applications, Naples, Italy, 2:215–220

Askarinejad A, Casini F, Bischof P, Beck A, Springman SM (2012b) Rainfall induced instabilities: a field experiment on a silty sand slope in northern Switzerland. Ital Geotech J 46(3):50–71

Askarinejad A, Beck A, Springman SM (2015) Scaling law of static liquefaction mechanism in geo-centrifuge and corresponding hydro-mechanical characterisation of an unsaturated silty sand having a viscous pore fluid. Can Geotech J 52:1–13. https://doi.org/10.1139/cgj-2014-0237

ASTM, D2487–06 Standard (2006) Standard practice for classification of soils for engineering purposes (Unified Soil Classification System). Annual Book of ASTM Standards, American Society for Testing and Materials, West Conshohocken

Bennett V, Abdoun T, Shantz T, Jang D, Thevanayagam S (2009) Design and characterization of a compact array of MEMS accelerometers for geotechnical instrumentation. Smart Struct Syst 5(6):663–679

Bishop AW (1959) The principle of effective stress. Teknisk Ukeblad 106(39):859–863

Bishop AW, Blight GE (1963) Some aspects of effective stress in saturated and partly saturated soils. Géotechnique 13(3):177–197

Borgatti L, Soldati M (2010) Landslides as a geomorphological proxy for climate change: a record from the dolomites (northern Italy). Geomorphology 120:56–64

Borja RI, White JA (2010) Continuum deformation and stability analyses of a steep hillside slope under rainfall infiltration. Acta Geotech 5(1):1–14

Brand EW (1981) Some thoughts on rainfall induced slope failures. In 10th International Conference on Soil Mechanics and Foundation Engineering, 373–376

Brönnimann C (2011) Effects of groundwater on landslide triggering, Nr. 5236. PhD thesis, EPFL, Lausanne, Switzerland

Brönnimann C, Stähli M, Schneider P, Seward L, Springman SM (2013) Bedrock exfiltration as a triggering mechanism for shallow landslides. Water Resour Res 49(9):5155–5167. https://doi.org/10.1002/wrcr.20386

Buchli T, Laue J, Springman SM (2016) Amendments to interpretations of SAAF inclinometer data from the Furggwanghorn rock glacier, Turtmann Valley, Switzerland: results from 2010 to 2012. Vadose Zone J 15. https://doi.org/10.2136/vzj2015.09.0132

Cascini L, Cuomo S, Pastor M, Sorbino G (2010) Modeling of rainfall-induced shallow landslides of the flow-type. J Geotech Geoenviron Eng ASCE 136(1):85–98

Casini F, Jommi C, Springman SM (2010) A laboratory investigation on an undisturbed silty sand from a slope prone to landsliding. Granul Matter 12(3):303–316

Casini F, Serri V, Springman SM (2013) Hydromechanical behaviour of a silty sand from a steep slope triggered by artificial rainfall: from unsaturated to saturated conditions. Can Geotech J 50:28–40

Cohen D, Schwarz M, Or D (2011) An analytical fiber bundle model for pullout mechanics of root bundles. J Geophys Res-Atmos 116(F03010). https://doi.org/10.1029/2010JF001886

Collins M, Knutti R, Arblaster J, Dufresne J-L, Fichefet T, Friedlingstein P, Gao X, Gutowski WJ, Johns T, Krinner G, Shongwe M, Tebaldi C, Weaver AJ, Wehner M (2013) Chapter 12 - Long-term climate change: projections, commitments and irreversibility. In IPCC (ed) Climate Change 2013: The Physical Science Basis. IPCC Working Group I Contribution to AR5, Cambridge University Press (Pub), Cambridge

Crozier MJ (2010) Deciphering the effect of climate change on landslide activity: a review. Geomorphology 124(3):260–267

Cruden DM, Varnes DJ (1996) Landslides: investigation and mitigation. Chapter 3—landslide types and processes. Transportation research board special report(247)

D'Onza F, Gallipoli D, Wheeler S, Casini F, Vaunat J, Khalili N, Laloui L, Mancuso C, Masin D, Nuth M, Pereira JM, Vassallo R (2011) Benchmark of constitutive models for unsaturated soils. Géotechnique 61(4):283–302

Daniel DE (1982) Measurement of hydraulic conductivity of unsaturated soils with thermocouple psychrometers. J Soil Sci Soc Am 20(6):1125–1129

Delage P, Romero E, Tarantino A (2008) Recent developments in the techniques of controlling and measuring suction in unsaturated soils Keynote Lecture, Proc. 1st Eur. Conf. on Unsaturated Soils, 33–52
Elia G, Cotecchia F, Pedone G, Vaunat J, Vardon PJ, Pereira C, Springman SM, Rouainia M, Van Esch J, Koda E, Josifovski J, Nocilla A, Askarinejad A, Stirling R, Helm P, Lollino P, Osinski P (2017) Numerical modelling of slope–vegetation–atmosphere interaction: an overview. Q J Eng Geol Hydrogeol 50(30):249–270. https://doi.org/10.1144/qjegh2016-079
Fischer C, López J, Springman SM (2003) Remediation of an eroded steep slope in weathered sandstone after a major rainstorm. In International Conference on Landslides, Hong Kong, 878–883
Frei C, Schöll R, Schmidli J, Fukutome S, Vidale PL (2006) Future change of precipitation extremes in Europe: an intercomparison of scenarios from regional climate models. J Geophys Res Atmos 111(D6):1–22. https://doi.org/10.1029/2005JD005965
Freudenthal AM (1966) Introduction to mechanics of solids. John Wiley and Sons, Inc. (Pub), New York
Gariano SL, Guzzetti F (2017) Evaluating the impact of climate change on landslide occurrence, hazard, and risk: from global to regional scale. EGU General Assembly Conference Abstracts 19:503
Griffiths D, Huang J, Dewolfe GF (2011) Numerical and analytical observations on long and infinite slopes. Int J Numer Anal Methods Geomech 35(5):569–585
Guzzetti F, Peruccacci S, Rossi M, Stark CP (2007) Rainfall thresholds for the initiation of landslides in central and southern Europe. Meteorog Atmos Phys 98:239–267
Harp EL, Wells WG, Sarmiento J (1990) Pore pressure response during failure in soils. Geol Soc Am Bull 102:428–438
Huggel C, Clague JJ, Korup O (2012) Is climate change responsible for changing landslide activity in high mountains? Earth Surf Process Landf 37(1):77–91
Jommi C (2000) Remarks on the constitutive modelling of unsaturated soils. In International Workshop on Experimental Evidence and Theoretical Approaches in Unsaturated Soils, Trento- Italy, 139–153
Khalili N, Khabbaz MH (1998) A unique relationship for the determination of the shear strength of unsaturated soils. Géotechnique 48(5):681–687
Krzeminska D, Bogaard T, van Asch TW, Van Beek L (2012) A conceptual model of the hydrological influence of fissures on landslide activity. Hydrol Earth Syst Sci 16(6):1561–1576
Labhart T (2005) Geologie der Schweiz, 210 pp. Ott Verlag, Bern
Ledieu J, de Ridder P, de Clerck P, Dautrebande S (1986) A method of measuring soil moisture by time-domain reflectometry. J Hydrol 88:319–328
Lehmann P, Gambazzi F, Suski B, Baron L, Askarinejad A, Springman SM, Holliger K, Or D (2013) Evolution of soil wetting patterns preceding a hydrologically induced landslide inferred from electrical resistivity survey and point measurements of volumetric water content and pore water pressure. Water Resour Res 49(12):7992–8004. https://doi.org/10.1002/2013WR014560
Leroueil S, Chu J, Wanatowski D (2009) Slope instability due to pore water pressure increase. The first Italian workshop on landslides, Naples, p 81–90
Marinho F, Take W, Tarantino A (2008) Measurement of matric suction using tensiometric and axis translation techniques. Geotech Geol Eng 26(6):615–631
McDonnell JJ (2003) Where does water go when it rains? Moving beyond the variable source area concept of rainfall-runoff response. Hydrol Process 17(9):1869–1875
Montgomery DR, Schmidt KM, Dietrich WE, McKean J (2009) Instrumental record of debris flow initiation during natural rainfall: implications for modeling slope stability. J Geophys Res Earth Surf (2003–2012) 114(F1)
Nuth M, Laloui L (2008) Effective stress concept in unsaturated soils: clarification and validation of a unified framework. Int J Numer Anal Methods Geomech 32:771–801
Öberg A-L, Sällfors G (1997) Determination of shear strength parameters of unsaturated silts and sands based on the water retention curve. Geotech Test J 20(1):40–48
Ochiai H, Okada Y, Furuya G, Okura Y, Matsui T, Sammori T, Terajima T, Sassa K (2004) A fluidized landslide on a natural slope by artificial rainfall. Landslides 1:211–220
Picarelli L (2000) Mechanisms and rates of slope movements in fine grained soils ISRM International Symposium, International Society for Rock Mech, 1618–1670
Picarelli L, Olivares L, Damiano E (2006) Discussion to ''Evaluation of landslide triggering mechanisms in model fill slopes.'' Take WA, Bolton MD, Wong PCP, Yeung FJ, and ''A fluidized landslide on a natural slope by artificial rainfall'' by Ochiai H, Okada Y, Furuya G, Okura Y, Matsui T, Sammori T, Terajima T, Sassa K. Landslides. 3: 269–272
Platt NH (1992) Fresh-water carbonates from the lower freshwater Molasse (Oligocene, western Switzerland): sedimentology and stable isotopes. Sediment Geol 78(1):81–99
Pollen N, Simon A (2005) Estimating the mechanical effects of riparian vegetation on stream bank stability using a fiber bundle model. Water Resour Res 41:W07025. https://doi.org/10.01029/02004WR003801
Rankine WM (1857) On the stability of loose earth. Philos Trans R Soc Lond 147:9–27
Schwarz M (2011) Hydro-mechanical characterization of rooted hill slope failure: from field investigations to fibre bundle modelling, Nr. 19124. DSc thesis, ETH, Zurich, Switzerland
Schwarz M, Lehmann P, Or D (2010) Quantifying lateral root reinforcement in steep slopes–from a bundle of roots to tree stands. Earth Surf Process Landf 35(3):354–367
Sinclair H (1997) Flysch to molasse transition in peripheral foreland basins: the role of the passive margin versus slab breakoff. Geology 25(12):1123–1126
Soga K, Alonso E, Yerro A, Kumar K, Bandara S (2016) Trends in large-deformation analysis of landslide mass movements with particular emphasis on the material point method. Géotechnique 66(3):248–273. https://doi.org/10.1680/jgeot.15.LM.005
Springman SM, Jommi C, Teysseire P (2003) Instabilities on moraine slopes induced by loss of suction: a case history. Géotechnique 53(1):3–10
Take WA, Bolton MD, Wong PCP, Yeung FJ (2004) Evaluation of landslide triggering mechanisms in model fill slopes. Landslides 1:173–184
Tang A-M, Askarinejad A, Cui YJ, Gentile F, Gowing J, Jommi C, Kehagia F, Keszeyné Say E, ter Maat HW, Lenart S, Lourenco S, Oliveira M, Osinski P, Springman SM, Stirling R, Toll D, Viterbo P (2018) Atmosphere–vegetation–soil interactions in a climate change context; impact of changing conditions on engineered transport infrastructure slopes in Europe. Quarterly Journal of Engineering Geology and Hydrogeology. https://doi.org/10.1144/qjegh2017-103
Toll DG (1990) A framework for unsaturated soil behaviour. Géotechnique 40(1):31–44
Towhata I, Uchimura T, Gallage C (2006) On early detection and warning against rainfall-induced landslides (M129). In: Sassa K, Fukuoka H, Wang F, Wang G (eds) Landslides, risk analysis and sustainable disaster management. Springer (Pub), Heidelberg, pp 133–139
Urciuoli G (2002) Strains preceding failure in infinite slopes. Int J Geomech 2(1):93–112
Urciuoli G, Picarelli L, Leroueil S (2007) Local soil failure before general slope failure. Geotech Geol Eng 25(1):103–122
Varnes DJ (1978) Slope movement types and processes. Transportation Research Board Special Report (176)
Wheatstone C (1843) The Bakerian lecture: an account of several new instruments and processes for determining the constants of a voltaic circuit. Philos Trans R Soc Lond 133:303–327
Yildiz A, Askarinejad A, Graf F, Rickli C, Springman SM (2015) Effect of roots and mycorrhizal fungi on the stability of slopes. In XVI European Conference on Soil Mechanics and Geotechnical Engineering, Edinburgh, UK, 1693–1698. https://doi.org/10.1680/ecsmge.60678
Zimmermann M, Mani P, Romang H (1997) Magnitude-frequency aspects of alpine debris flows. Swiss Geol Soc (Eclogae Geol Helv) 90:415–420

Electronic supplementary material The online version of this article (https://doi.org/10.1007/s10346-018-0994-0) contains supplementary material, which is available to authorized users.

A. Askarinejad (✉)
Faculty of Civil Engineering and Geosciences,
TU Delft,
Stevinweg 1/PO-box 5048, 2628 CN Delft/, 2600, GADelft, The Netherlands
Email: A.Askarinejad@tudelft.nl

A. Askarinejad · S. M. Springman
IGT, ETH Zurich, Stefano-Franscini-Platz 5,
8093, Zurich, Switzerland

S. M. Springman
e-mail: sarah.springman@igt.baug.ethz.ch

D. Akca
Department of Civil Engineering,
Isik University,
TR-34980 Sile, Istanbul, Turkey
e-mail: akca@isikun.edu.tr

D. Akca
Institute of Geodesy and Photogrammetry, ETH,
Zurich, Switzerland